Precision measurements of K and L transitions in xenon: Experiment and theory for the K, L, and M levels

T. Mooney*

National Institute of Standards and Technology, Gaithersburg, Maryland 20899

E. Lindroth

Department of Physics, Chalmers University, Göteborg S-41296, Sweden

P. Indelicato,[†] E. G. Kessler, Jr., and R. D. Deslattes

National Institute of Standards and Technology, Gaithersburg, Maryland 20899

Wavelengths of xenon L-series x-ray lines were measured with high accuracy using a double flat-crystal vacuum spectrometer. Wavelengths of the more prominent xenon K-series lines which had been obtained previously are fully reported and corrected for recent scale changes. Energies of forbidden transitions, such as $1s$-$2s$, have been determined from redundant combinations of K- and L-series measurements. Transition energies have been calculated relativistically including relaxation to all orders, correlation to second order, and QED effects. Agreement between experiment and theory is of the order of 0.1 eV, except for transitions involving $3s$ holes where it is 1 eV.

PACS number(s): 31.20.Di, 31.30.Jv, 12.20.Fv

I. INTRODUCTION

Recent progress in theoretical description of atoms with inner-shell vacancies [1,2] and improved systematic experimental studies—including very recent data from the rare earths in the L series, and Se in the K series [3]—have shown numerical consistencies near or below the 1-eV level over wide ranges in Z excluding only certain of the transuranic elements [1,2]. Such comparisons of atomic theory with data largely obtained from condensed targets at this level of sensitivity are not easily justified in advance. Specifically, open-shell atoms, already giving some difficulty in the free-atom calculations, are certainly modified in condensed phases, where at least the screening of inner shells is changed by the outer electrons. Further complications arise in calculations of inner-shell term energies since the atom now has two open shells. In spite of such cautions the comparisons exhibit the remarkable consistencies noted above. However, more robust comparisons are possible in the absence of incomplete outer shells and where spectra can be conveniently obtained experimentally in the gas phase, i.e, the rare-gas atoms. Among these, xenon is particularly attractive since its nuclear charge is sufficiently high that relativistic and quantum electrodynamic effects are large compared to the precision and accuracy of practical comparisons between theoretical calculations and experimental data.

Experimental data on the x-ray spectra of atomic xenon have been both sparse and weak. In particular, data in Bearden's compilation [4] are, for the most part, empirical interpolations from semi-Moseley diagrams anchored by nearby data from solid targets. The assigned uncertainties are (properly) rather large (typically in excess of 1.4 eV for the K-series lines and 0.3 eV for the $L\alpha_1$ line, which is the only tabulated L-series line). Both the procedure used for these estimations and their uncertainties render them unsuitable for useful comparisons with currently available theoretical calculations. About ten years ago some new data of high quality were obtained for the K series of xenon as part of a larger mid to high-Z x-ray wavelength program [5]. In a later summary review [6] the numerical results were compared to a reference theory due to Grant and co-workers [7,8]. This reference theory was chosen because it was in a form suitable for use by nonspecialists and was based on the multiconfiguration Dirac-Fock (MCDF) procedure due to Desclaux [9,10].

In view of the important role played by xenon in assessing the accuracy of calculations, we have extended and improved on both the theoretical and experimental situations with results which are the subject of this report. On the theoretical side, our calculations use the latest improvements of the MCDF procedures (see, for example, Ref. [11]) together with relativistic many-body perturbation calculation of correlations and core-core corrections. On the experimental side, we report the methods used to obtain the earlier K-series measurements and an entirely new set of L-series measurements. The L-series data are more complete and accurate than those reported previously and are associated with detailed error budgets. Because the inclusion of dynamic effects results not only in line shifts but also in significant changes in the line profiles, we give, for the first time, detailed profiles of all prominent L-series emission lines. Prior to the measurement of the L-series data reported here, LaVilla used the same apparatus, but with less rigorous procedures, to obtain experimental values for peak locations for the same set of L lines [12].

II. EXPERIMENTAL PROCEDURES

Measurements reported here are based on the use of diffraction crystals with accurately known lattice periods (*d* spacings) in angle-measuring machines calibrated from first principles. While the general procedures are outlined in previous reviews [13,14], the specific problems associated with the widely different wavelength regions as well as recent developments lead us to outline these methods in some detail in the Appendices. In both the *K*-series and *L*-series spectra, instrumental resolution has been realized in which the associated line broadening is very much smaller than the intrinsic linewidths. In addition, the accuracies obtained are sufficient both to exhaust the available statistical precision and to reach the limits imposed by model-dependent uncertainties in the interpretation of such spectra.

A. *L*-series measurements

The *L*-series spectra were excited by radiation from a conventional demountable x-ray source with a chromium anode. Spectra were analyzed by a vacuum two-crystal spectrometer using Ge(220) crystals with accurately known lattice spacing (see Appendix A). The instrument's second axis was equipped with a high-resolution angle encoder which was accurately calibrated as described in Appendix B. The following paragraphs give further details on the experimental procedures and corrections required.

1. Source and excitation

Figure 1 shows the source region including the primary anode, the gas cell, and windows needed to isolate the spectrometer vacuum and x-ray tube vacuum from the
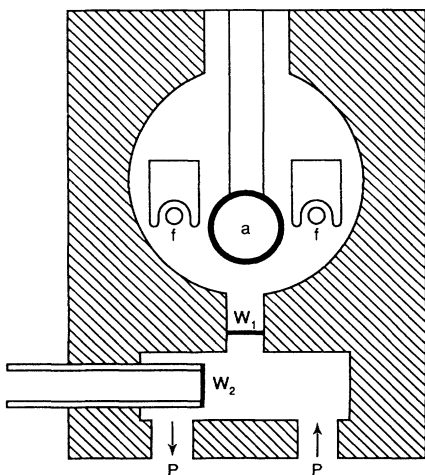
gas. Chemically pure xenon gas at pressures near 16.7 kilopascal (125 Torr) flowed slowly through the cell. Gas density was stabilized to about 0.1% by means of a pycnostat [15]. The high-power demountable x-ray tube [16] used a chromium primary anode operated at 16 kV with a standing current of about 180 mA. Both current and voltage were highly regulated to permit slow step-scanned data acquisition. From the reproducibility of repeated scans, these measures were evidently effective and no other significant time dependences appeared.

2. Spectrometer and data acquisition

The basic spectrometer has evolved from its original form [17] principally with the addition some years ago of high-resolution angle encoders. These have 12 000 optical cycles per revolution. The four moiré readers give pseudo-sin/cos signals which are summed to give a resolver response which should be independent of centering errors, etc. (see Appendix B). By rapid multisampling of these signals and conversion of the sin/cos amplitude to a phase, a readout precision of below 0.1 arcsec is obtained. The data reported here are based on new calibration procedures which are both more robust and more detailed than those used previously.

As shown schematically in Fig. 2, the measurement sequence involves repeated acquisition of profile scans in the nondispersive (parallel) "minus" configuration and in the dispersive (antiparallel) "plus" configuration. Except for certain important corrections (see below), the primary datum is the angular interval between the plus and minus diffraction features. For the customary directions of rotation, this interval is $(2\pi - 2\theta_B)$ where θ_B is the Bragg angle [18]. The nondispersive profile is always symmetrical and narrow compared with the dispersive profile; its measurement serves to locate the first crystal's position. The fully dispersed profile in the plus position contains

FIG. 1. Schematic of the x-ray tube and xenon target. Electrons from the directly heated filament, *f*, are accelerated to the water cooled anode, *a*, forming a broad focal spot opposite the exit window, w_1. The reentrant window, w_2, enables the spectrometer to view the fluorescing gas volume through a minimum path of unexcited gas.
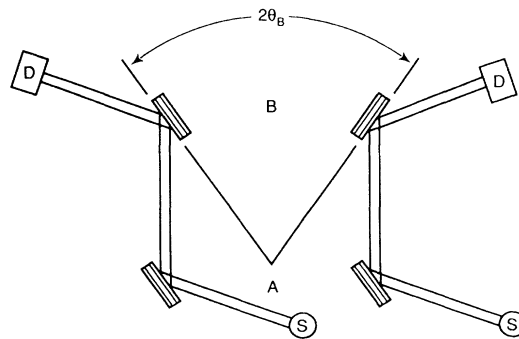
FIG. 2. Vacuum reflection double flat-crystal spectrometer. The left and right parts of the figure illustrate the nondispersive and dispersive configuration of the crystals *A* and *B*. The angular interval, $2\theta_B$, is illustrative only since the corresponding rotation is not physically realizable for the reflection geometry shown (see text). It correctly suggests that only the dihedral angle for the second, *B*, crystal enters the wavelength determination, independent of refined considerations of source and detector position, provided the crystals are fully illuminated.

not only instrumental broadening, including the vertical-divergence window (see below), but also the line profile. If the latter has some degree of symmetry or is otherwise modelable, then unique locations can be assigned to the overall profile or its components. In the present work, we assign these locations on the basis of peak positions, derived from global fits to the profiles.

Data were acquired by summing many individual scans, typically 30 scans over 50 points for 10 min for the plus position and six similar minus-position scans. The individual scans were summed to obtain a profile for subsequent fitting. This protocol averages over instrumental variations (e.g., anode voltage and current, target deterioration, etc.,) which are not correlated with the scanning period. Such a protocol involves, however, some risk of data deterioration if the angular scale is unstable or insufficiently reproducible. It appears that the angular reproducibility of 0.3 arcsec is sufficiently small relative to the calibration accuracy (0.86 arcsec) and the

step interval (3.6 arcsec) that it does not cause deterioration of the data reported.

3. Results and systematic corrections

Composite profiles for the principal *L*-series emission lines of xenon are shown in Fig. 3. Minus-position profiles are superimposed on the plus-position curves to indicate the approximate instrumental passband in relation to the natural linewidth. The asymmetry evident in certain profiles is due to the presence of nearby lines.

The plus- and minus-scan composite profiles were fit separately to Voigt functions (in the case of symmetric lines), using a curve-fitting program built around the variable-metric, gradient minimizer, MINUIT [19]. An uncertainty was estimated for each parameter's best-fit value by finding how much it had to change to increase the best-fit χ^2 value by unity with all other parameters freely varied to minimize χ^2. For certain of the weaker
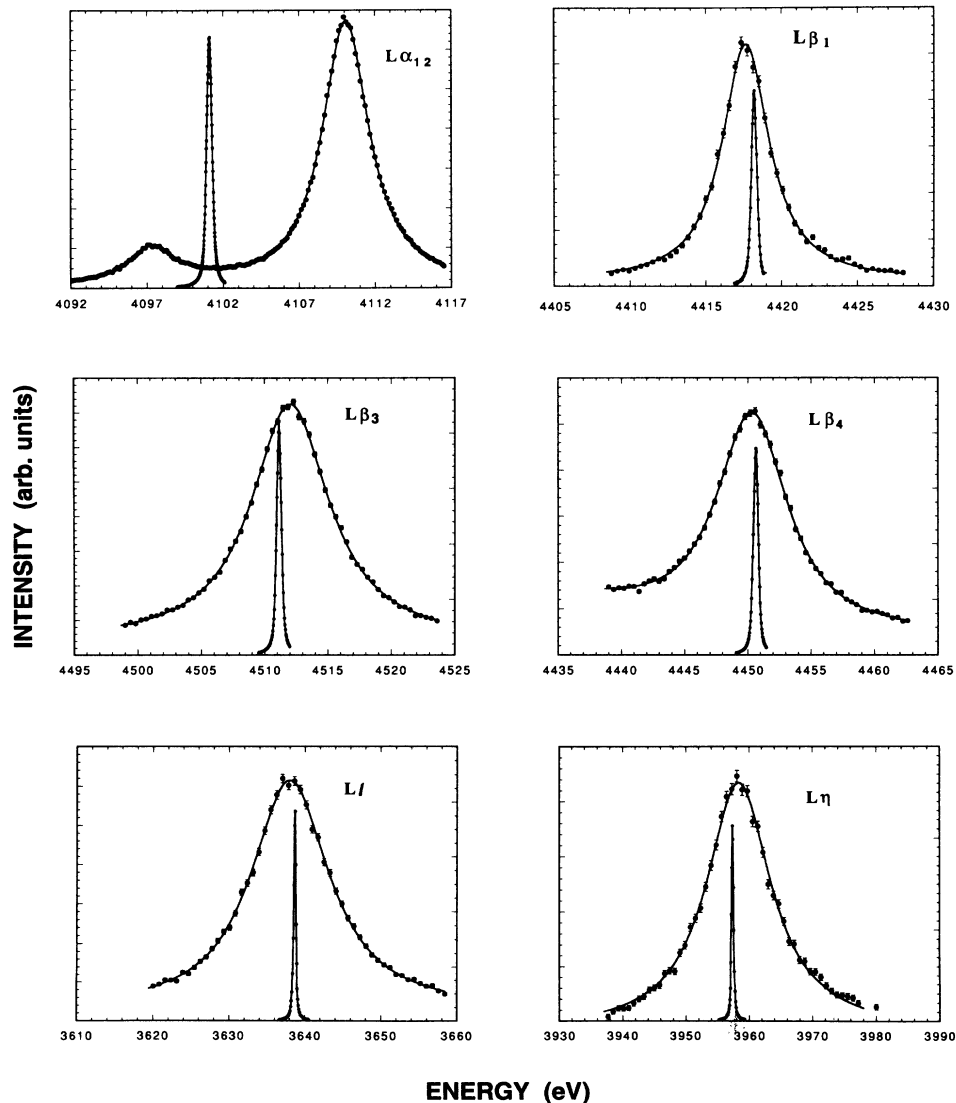
FIG. 3. Experimental *L* x-ray spectra. The narrower profile shows the minus-position rocking curve which is indicative of the available spectroscopic resolution.

lines, fitting uncertainties dominate the error budget.

Raw values of the Bragg angle emerging from the above fitting procedures require two major corrections. First, there is a shift due to finite vertical divergence. Actually, this requires convolution of the vertical-divergence window function with the spectrometer's diffraction profile; however, for small values of vertical divergence and relatively-modest-accuracy targets as is the case here, it is sufficient to consider the peak shift [20]:

$$\Delta\theta = S\tan(\theta) \ , \quad S = \frac{(a^2+b^2)}{24L^2} \ , \tag{1}$$

where a and b are the vertical apertures at the source and detector assumed to be separated by L. For the geometry used, this shift is approximately 3.6 ppm, hence a conservative estimate of 10% for its uncertainty means that this effect produces a nearly negligible contribution to the error budget.

A larger and more uncertain correction is required to take account of the index of refraction. When this effect is included, the modified Bragg equation is [21]

$$\lambda = 2d[1-4d^2(\delta/\lambda^2)]\sin\theta_B \ , \tag{2}$$

where δ is the decrement in index of refraction. The quantity (δ/λ^2) is slowly varying and can be estimated from the Cromer-Liberman calculations [22]. For Ge in the region spanned by the xenon L spectra, this correction is approximately 101 ppm. There is some difficulty in assigning a meaningful uncertainty to this correction. From experience in other wavelength regions we judge that 5% is a reasonable estimate but feel that this should be reexamined before interpretations are undertaken beyond the relatively modest level reported here.

The actual reduction of a corrected profile interval to a wavelength value requires finally that the Ge (220) lattice period be assigned a numerical value which actually varies from day to day due to temperature drifts. The base value of 0.200 033 913 nm at 22.5 °C is discussed in Appendix A. Crystal temperatures were monitored by small thermistors calibrated with respect to a platinum resistance thermometer. Lattice expansion was estimated using a value of 5.95 ppm/°C for Ge [13]. Temperature values were typically in the range 25–27 °C and drifted by about 0.3 °C during the data acquisition period for a single L-series line.

The effect of temperature drift during a measurement on the extracted wavelength value was assessed by performing a computer simulation: An artificially constructed line profile was smeared, according to a measured temperature distribution, and fit by the same procedure used for actual data. We expected and found a linear dependence of the extracted wavelength on the average of the temperature distribution. We did not find any significant dependence on the standard deviation of the distribution. We have found that the uncertainty in extracted wavelength is 0.2 ppm, which is negligible compared to other uncertainties involved in the fitting procedure.

A sense of the relative importance of the various systematic corrections and their uncertainties to the overall error estimate can be gained by inspection of Table I. Here we have indicated both the magnitude of the correction and its uncertainty as well as the statistical and fitting errors.

Table II gives the wavelengths and total uncertainties in eV for the lines measured. The present results represent the most accurate measurements of these prominent lines and, in all cases, claim a level of imprecision below 0.05 eV.

TABLE I. Corrections to transition energies for xenon L-series measurements. Magnitudes and their uncertainties (in parentheses) are given in parts per million; the sign of a correction describes its effect on the energy of an x-ray line.

Line	Mean temp. (°C)	Refract. index[a]	Vertical diverg.[b]	Crystal temp.[c]	Angle calib.[d]	Fit[e]	Total
$L\alpha_1$	26.65(24)	101 (5)	3.6 (0.4)	−24.7 (0.2)	(1.8)	(0.9)	(5.4)
$L\alpha_2$	26.65(24)	101 (5)	3.6 (0.4)	−24.7 (0.2)	(1.8)	(3.1)	(6.2)
$L\beta_1$	26.15(3)	101 (5)	3.6 (0.4)	−21.7 (0.2)	(2.1)	(3.8)	(6.6)
$L\beta_3$	26.18(10)	101 (5)	3.6 (0.4)	−21.9 (0.2)	(2.2)	(2.9)	(6.2)
$L\beta_4$	26.70(20)	101 (5)	3.6 (0.4)	−25.0 (0.2)	(2.2)	(5.2)	(7.6)
$L\eta$	26.75(50)	101 (5)	3.6 (0.4)	−25.3 (0.2)	(1.7)	(12.0)	(13.1)
Ll	26.50(8)	101 (5)	3.6 (0.4)	−23.8 (0.2)	(1.3)	(9.6)	(10.9)

[a]Corrections to the transition energy due to the decrement in the index of refraction [see Eq. (2)]. Values of δ taken from the work of Cromer and Liberman [22].

[b]Correction to the Bragg angle given by Eq. (1) in the text. This form takes account of the facts that the vertical-divergence correction vanishes for the symmetric minus reflection and that the quantity actually measured is twice the Bragg angle.

[c]The d spacing of the Ge crystals used for xenon measurements is customarily given at 22.5 °C (see Appendix A) while the xenon measurements were taken at the indicated average temperatures. The uncertainties in the table reflect the absolute calibration uncertainty of the thermistors (best estimate: 0.03 °C) and the thermal expansion coefficient of Ge.

[d]The values indicated were obtained by converting the estimated scale uncertainty of 0.3 arcsec to an energy value and dividing this by the mean energy of the transition. The magnitude of the calibration correction is well defined for a single angle measurement, but not for the set of measurements involved in an angular scan over many periods of the raw error. We assume that this effect is included in the "fit" uncertainty.

[e]The fitting uncertainty expresses the sensitivity of the χ^2 goodness-of-fit to the peak-location fit parameter, and includes the effects of correlations with other fit parameters. For the $L\alpha_2$ line, the principal correlation was with the peak location of the $L\alpha_1$ line. For the $L\beta_4$ line, there was a small correlation with the background slope.

TABLE II. Xenon *L* x-ray lines.

Line	Energy (eV)	Uncertainty (eV)
$L\alpha_1$	4110.09	0.02
$L\alpha_2$	4097.38	0.03
$L\beta_1$	4417.67	0.03
$L\beta_3$	4512.03	0.03
$L\beta_4$	4450.33	0.03
$L\eta$	3958.37	0.05
Ll	3638.01	0.04

B. K-series measurements

The Xe *K*-series x-ray spectra were measured earlier as part of a broader program which included elements $47 \le Z \le 92$ [5]. In that study, all targets were solid except Xe, and thus the Xe x-ray wavelengths provided an estimate of the wavelength shift of inner-shell x rays produced in condensed-phase and gas-phase targets. The *K*-series x-ray spectra were produced in a high-pressure gas cell excited by a 2.5-MeV electron beam from a Van de Graaff accelerator. The spectra were analyzed by a transmission two-crystal spectrometer using Si crystals in symmetric Laue diffraction. The following paragraphs describe this instrument and the associated measurement procedures in more detail.

1. Source and excitation

The Xe *K* x rays were produced by electron bombardment of Xe gas contained in a high-pressure thin-window gas cell. The electrons were produced at the 4-MeV electron Van de Graaff located at NIST, Gaithersburg. Although photon yield increases with electron energy, the accelerator was operated at an electron energy of ≈ 2.5 MeV in order to achieve continuous stable operation [23]. The high-pressure gas cell had a 0.5-mm-thick Al window and a volume of ≈ 5 cm^3. It was water cooled and was filled and sealed with Xe up to pressures of $\approx 2.5 \times 10^6$ Pa. The electron beam was focused on the window of the gas cell, and its position and shape was monitored using a fluorescent coating and television camera. When properly focused the beam was a circle 2–3 mm in diameter. The cell was electrically isolated from the vacuum chamber so that the beam current on the target could be measured with an electrometer and used to normalize the measured x-ray intensity. Typical beam currents were 40–70 microamperes and varied by at most a few percent during the course of a profile scan.

2. Transmission two-crystal spectrometer

The *K*-series wavelengths were measured with a two axis flat-crystal transmission spectrometer equipped with nearly perfect Si crystals whose lattice spacing has been measured in terms of an optical-wavelength standard (see Appendix A). This instrument measures the angles through which the x rays are diffracted. The angular rotation of each crystal is measured with a Michelson polarization-sensitive angle interferometer having a readout uncertainty of a few tenths of a milliarcsec. The interferometers are calibrated on an absolute basis by a protocol which uses a 24-sided optical polygon (see Appendix B). By combining the absolute-angle measurements with the optically based lattice-spacing measurements, wavelengths consistent with the optical-wavelength scale and thereby with the scale used in theoretical calculations result. This spectrometer was developed for high-energy γ-ray wavelength measurements where sub-ppm measurements of Bragg angles of a few tenths of a degree are needed. More details concerning this spectrometer are available in Ref. [13]. The Si 220 planes were used for all the measurements and the Bragg angles for the $K\alpha$ and $K\beta$ transitions ranged from 5.5° to 6.3°.

3. Data acquisition and analysis

The x-ray profiles were recorded by step scanning the second crystal through the diffraction maxima using 25–50 steps per profile and counting times of 15–60 sec per step. The measurement sequence was similar to that used for the *L*-series data and involved profile recording with the two crystals in the parallel (nondispersive) and antiparallel (dispersive) positions. Except for a small correction due to the finite vertical-divergence window, the angular interval between the second crystal positions for the parallel and antiparallel diffraction profiles is $2\theta_B$ where θ_B is the Bragg angle.

The profiles were fit to model functions using a nonlinear least-squares procedure. The model for the parallel profiles was a Lorentzian function while the model for the antiparallel profiles was a Lorentzian function convoluted with a vertical-divergence function [13]. The parameters for the vertical divergence are known from the geometry of the source and Soller collimators. The vertical-divergence function makes only a minor contribution to the composite profile because the x-ray lines have large intrinsic widths. Within the statistical uncertainty, the dispersive profiles are fit equally well with just a Lorentzian function and return parameters which differ by less than the measurement uncertainty. Nevertheless, the profile, including the vertical-divergence function, was used to obtain the reported results. Because the recorded $K\beta_1$ and $K\beta_3$ profiles slightly overlap, the $K\beta$ data were fit with a two-component model which adjusted the parameters for the two components simultaneously.

4. Experimental results; comparison with prior data

In Table III, the experimental energy values for the $K\alpha$ and $K\beta$ transitions are reported. These values differ from those given in Refs. [5] and [6] by ~ 0.3 eV because of the use of a more recent wavelength-energy conversion factor [24] and the correction of the value used for the Si lattice spacing (see Appendix A).

III. THEORETICAL CALCULATION

The study of inner-shell vacancies has been carefully documented by Crasemann and co-workers [25,26].

TABLE III. Xenon K x-ray lines.

Transition	Energy (eV)	Uncertainty (ppm)
$K\alpha_2$	29 458.16	1.8
$K\alpha_1$	29 778.69	3.2
$K\beta_3$	33 563.10	3.6
$K\beta_1$	33 624.13	3.6

Chen *et al.* [27] have compared experimental and theoretical results for binding energies of most $n = 1, 2, 3,$ and 4 levels over a wide range of Z. The Dirac-Hartree-Slater method was applied and corrections due to the Breit interaction were added on that level. Coster-Kronig fluctuations were found to be especially important for vacancies in, e.g., $2s$ [28], $3s$, and $4s$ where the presence of a nearby p state makes possible a virtual Auger-like transition with small energy denominator and a large radial overlap. The correction due to correlation was, in Ref. [27], added from nonrelativistic calculations and self-energy corrections were obtained with an effective-charge screening procedure. The comparisons with experiment, given in figures only, show small deviations for light systems but typically 3–7 eV for medium to high Z. The deviations were attributed to the uncertainty in the radiative corrections and the incomplete treatment of correlation.

During recent years there has been a substantial development in the field of relativistic atomic calculations. All many-body effects can now be treated in a relativistic framework. That applies to correlation, due to both Coulomb and Breit interaction, as well as to the core-core interactions of which the Coster-Kronig effects constitute an important subclass. The treatment of QED effects in many-body systems has been refined, compared to the previous effective-change methods [29]. In the present work we have made use of these developments and it has been possible to reduce the deviations from experiments considerably. The radiative corrections are discussed in Sec. III A and the many-body part of the calculation in Sec. III B. The difference compared to the calculation by Chen *et al.* [27] is discussed further in Sec. III D.

In this work we have evaluated the zeroth-order energy, retardation contributions, and QED corrections with the most recent version of Desclaux's Dirac-Fock program [10,11]. We included full exchange and relaxation, using the most recent values for fundamental constants [24]. A Fermi model is used for the nucleus and the grid on which the wave functions are tabulated has 59 points inside the nucleus, is logarithmic near the origin, and linear at infinity, in order to get very precise wave functions in the region where they will contribute most to radiative corrections. The parameters for the Fermi distribution are calculated using a spherical mean radius from Ref. [30]. The magnetic interaction is included in the self-consistent-field process. While this gives a relatively small change in the Dirac-Fock energy of the atom [31], it does change the wave function at the origin to the extent that the vacuum-polarization contribution is slightly affected. Complete retardation in the Coulomb gauge has been evaluated as a first-order perturbation. The use of the Coulomb gauge in such a nonlocal method as the Dirac-Fock one is very important to avoid spurious contributions, as has been shown theoretically [32–34] and by comparing high-precision two-electron MCDF results with experiment [35].

Many-body effects beyond the relaxation, involving single (e.g., Auger or Coster-Kronig fluctuations) and double excitations (correlation) have been treated to second order, taking both Coulomb and Breit interactions into account. The calculation was done using relativistic many-body perturbation theory (MBPT) with a discretized Dirac-Fock basis set, complete on the chosen grid, as described in Refs. [36] and [37]. The relaxation contribution from this procedure has been checked against the fully relaxed Dirac-Fock values and found in very good agreement. The MBPT calculation of inner-shell vacancies and Auger shifts was pioneered by Kelly and co-workers [38,39] on the K shell of neon.

A. Radiative corrections

The next main difficulty in such a calculation lies in the evaluation of radiative corrections. For the vacuum-polarization contributions, potentials of order $\alpha(Z\alpha)$—the Uehling potential—of order $\alpha(Z\alpha)^3$, and of order $\alpha^2(Z\alpha)$—the Källén and Sabry potential—have been used in first-order perturbation with Dirac-Fock wave functions, accounting for both the finite nuclear size and screening corrections. Numerical results obtained through this procedure have been checked against the one-electron results of Ref. [30] for the first two contributions and against Ref. [40] for the last contribution, and found to be very accurate. The one-electron self-energy [41,42] corrected for the finite nuclear size as in Ref. [30] has been included. Precise accounting for the finite nuclear size in the evaluation of all radiative corrections is essential in the heavy atom region. For shells with $n \geq 3$, an n^{-3} scaling has been used to get self-energy corrections. It has been shown [43] that such a scaling very accurately reproduces direct evaluation.

To account for the so-called screening correction to the self-energy, for which there is no effective potential, an approximate method based on semiclassical arguments has been used. This method provides an effective potential to correct the lowest order in $(Z\alpha)$ of the self-energy for changes in the electronic density at the nucleus. This method has been extensively checked against experiment at low and medium Z in two- [29,35,44] and three-electron ions [35,45], and previous theoretical results [46,47]. In other calculations done for very heavy elements [27] the self-energy screening correction was evaluated using an effective-Z method which lacks rigorous justification and has been found to overestimate the screening corrections. A QED calculation of this screening is under way, and preliminary numbers for lithium-like uranium have been reported [48]. Those numbers are in reasonable agreement with our semiclassical evaluation. This shows that the high-order contributions in $(Z\alpha)$ do not play an important role for the self-energy screening, although they are of prime importance for the hydrogenic self-energy.

B. Many-body effects

The lowest-order contribution to the level shift of the energy of a hole state is the negative of the eigenvalue of the Dirac-Fock Hamiltonian, which according to Koopman's theorem is the work required to remove one electron from the system under the assumption that the other electrons remain unaffected. The Dirac-Fock Hamiltonian can be generalized to include the Breit interaction thus taking the exchange of virtual transverse photons in the low-energy limit into account. The Breit interaction contributes in the same order as relativistic corrections to the Coulomb interaction, i.e., $\alpha^2 Z_{\text{eff}}^3$. The retardation of the electromagnetic interaction beyond the Breit interaction contributes in the same order as many-particle QED effects $\alpha^3 Z_{\text{eff}}^3$ and has been discussed above.

Many-body effects, which take into account that the other electrons are not unaffected by the creation of a core hole, are illustrated in Figs. 4–6. The diagrams in Fig. 4 show second-order correlation which involves double excitations. The dashed lines denote the interactions: either two orders in the Coulomb interaction or one order in Coulomb and one in the Breit interaction. Correlation enters in at the order of magnitude unity with leading relativistic contributions of order $\alpha^2 Z_{\text{eff}}^2$, which is also the order of magnitude where the Breit correlation enters. The sum over excited states r and s in Fig. 4 runs over positive-energy states only, and we note that the corresponding diagrams which include negative-energy states, which are neglected, contribute in relative order $\alpha^3 Z_{\text{eff}}^3$. The sum over excited states r and s should in principle extend to all possible angular momenta, but in practice it is truncated after $l = 10$; the contribution from higher l values is estimated to be less than 0.1 eV. Higher-order correlation will contribute in relative order $1/Z_{\text{eff}}$, and may give contributions at the 0.1-eV level for the $3d$ hole states.

The diagram in Fig. 5 shows second-order single excitations. In the intermediate state there are two core holes and one excited single-particle state. If one of these holes is in the same orbital as the hole in the initial state and if the other core hole and the excited state have the same j and l value ($|a\rangle = |h\rangle$, $js = jb$, and $ls = lb$ or vice versa in Fig. 5) it is referred to as relaxation. When the relaxation is treated to all orders, i.e., including the class of diagrams in Fig. 6, the remaining electrons will experience the correct charge and a subclass of Fig. 6 assures that all
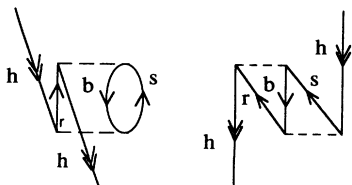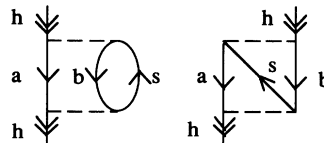
FIG. 5. Second-order contribution involving a single excitation. If either $|a\rangle = |h\rangle$ and $jb = js$, $lb = ls$ or $|b\rangle = |h\rangle$ and $ja = js, la = ls$ these diagrams constitute the lowest-order contribution to the relaxation. If on the other hand these restrictions are not fulfilled the contributions from the diagrams are either called core-core contributions, that is, when the energy denominator is negative for all possible excited single-particle states, $|s\rangle$, or Auger shift when the energy denominator changes sign during the summation over excited states. In the latter case the intermediate state is autoionizing. The calculation includes all possible contributions of the type illustrated in this figure.

spherically averaged readjustments have taken place. Also the relaxation due to the Breit interaction is treated to all orders.

If the restrictions in the summation over core holes and excited states used to calculate the relaxation are abandoned, the initial hole in Fig. 5 is allowed to fluctuate to two other orbitals and, further, all possible l and j values are included for the excited single-particle state. The diagrams in Fig. 5 naturally separate into two classes depending on whether the sum of core electrons on the intermediate level has a higher or lower energy than the initial hole state. When the intermediate state is more tightly bound than the initial state these core-core diagrams are straightforward to calculate. Especially important contributions arise when both the electrons in the intermediate state lie above the hole, since then the energy denominator can be very small. For example, a $2s$ hole that is shifted by -8.3 eV by core-core effects gets large
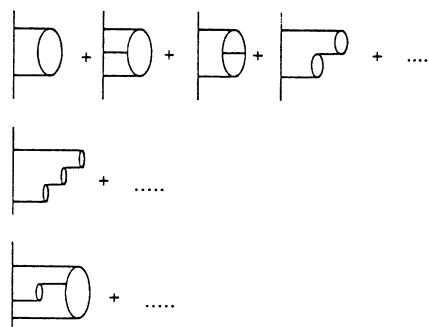
FIG. 6. Illustration of the type of diagrams which are included when the diagrams in Fig. 5 are iterated to all orders. The fully relaxed result includes all contributions of this kind where one of the states on each level is equal to $|h\rangle$ and if also the further restrictions explained for the lowest-order diagram in Fig. 5 are fulfilled. For the diagrams indicated on the third line only the monopole terms are included. The higher-order core-core result includes all diagrams on the first and second line with nonautoionizing intermediate levels which are not already included in the relaxation. Exchange versions are included for all diagrams.

FIG. 4. Second-order correlation involving double excitations. The dashed lines denote the interactions; either two orders in Coulomb interactions or one order in the Coulomb and one in the Breit interaction.

contributions from $(2p3d)nf$ intermediate states due to both a small energy denominator and large overlaps of the nonlocalized d and f orbitals. Also when one of the electrons in the intermediate states lies below the hole the contribution may be significant. A $2p_{3/2}$ hole is shifted -2.7 eV and large contributions come from intermediate states as $(2s3d)nf$ and $(2s2p_{3/2})nd$. In the latter case there is still a hole in $2p_{3/2}$ in the intermediate state, but the angular momenta of the excited state exclude it from the relaxation. The most important contributions, like the examples given here, are all dipole terms. The calculation includes, however, all possible contributions illustrated in Fig. 5.

The core-core contributions have also been iterated to all orders, generating the diagrams indicated on the first and second lines in Fig. 6. Significant contributions are found especially for the $2s$ hole but also for $3s$ and $3p_{1/2}$ holes. The comparisons with experiment for the transitions to or from $2s$ are improved by one order of magnitude and show only a 0.1-eV deviation when these higher-order contributions are included.

If, on the other hand, the energy of the intermediate state of two core holes is higher than the energy of the initial state, then the intermediate state is autoionizing and special care has to be taken. The presence of an Auger channel will give rise to a level shift of the energy, obtained as the principal value of the divergent integral. The size of this Auger shift depends, as in the core-core case, mainly on how close the initial-state hole and the intermediate-state holes are in energy. The $3s$ hole shows a large Auger shift, 2.8 eV, largely due to intermediate holes in $3p$ and $4d$. The Auger shift is treated by a method suggested in Ref. [49] where the matrix elements, obtained numerically, are fitted to a polynomial and the integral, which extends over a pole in the energy denominator, is carried out analytically. The Breit contributions to the core-core and Auger shifts are less then 0.1 eV and have not been included in Tables IV and V.

TABLE IV. Contributions to theoretical ionization energies (eV). The number of decimal places reflects the numerical accuracy only.

Level	$1s_{1/2}$	$2s_{1/2}$	$2p_{1/2}$	$2p_{3/2}$		
Dirac-Fock (Coulomb)	34 755.77	5509.33	5161.43	4835.57		
Relaxation	-70.00	-37.80	-41.66	-40.58		
Dirac-Fock (Breit)	-80.71	-7.64	-13.05	-8.81		
Breit relaxation	-1.46	-0.08	-0.07	-0.11		
Higher-order retardation	0.78	-0.08	0.00	0.34		
Correlation	1.80	1.99	3.05	3.02		
Breit correlation	0.95	0.21	0.31	0.24		
Core-core	-0.32	-8.29	-3.18	-2.75		
Higher-order core-core	0.02	0.96	0.15	0.11		
Auger shift	0.35	-0.06	0.23	0.53		
Self-energy	-50.98	-7.73	-0.09	-0.75		
Self-energy screening	2.91	1.69	0.47	0.57		
Vacuum polarization $\alpha(Z\alpha)$	6.95	0.81	-0.02	-0.04		
Vacuum polarization $\alpha(Z\alpha)^3$	-0.16	-0.02	0.00	0.00		
Vacuum polarization $\alpha^2(Z\alpha)$	0.06	0.01	0.00	0.00		
Total ionization energy	34 565.95	5453.30	5107.57	4787.34		
Level	$3s_{1/2}$	$3p_{1/2}$	$3p_{3/2}$	$3d_{3/2}$	$3d_{5/2}$	
Dirac-Fock (Coulomb)	1170.37	1024.77	961.25	708.13	694.90	
Relaxation	-16.96	-17.56	-17.10	-18.82	-18.68	
Dirac-Fock (Breit)	-1.10	-2.03	-1.23	-0.63	-0.28	
Breit relaxation	0.00	-0.01	0.00	0.00	0.00	
Higher-order retardation	-0.02	-0.01	0.06	-0.01	0.00	
Correlation	1.98	2.60	2.60	4.30	4.29	
Breit correlation	0.00	0.00	0.00	0.00	0.00	
Core-core	-6.10	-5.65	-4.95	-3.26	-3.15	
Higher-order core-core	0.38	0.29	0.22	0.25	0.23	
Auger shift	2.80	0.74	0.70	0.04	0.04	
Self-energy	-2.34	-0.07	-0.25	0.04	-0.04	
Self-energy screening	1.12	0.15	0.23	0.08	0.13	
Vacuum polarization $\alpha(Z\alpha)$	0.16	-0.01	-0.01	-0.01	-0.01	
Vacuum polarization $\alpha(Z\alpha)^3$	0.00	0.00	0.00	0.00	0.00	
Vacuum polarization $\alpha^2(Z\alpha)$	0.00	0.00	0.00	0.00	0.00	
Total ionization energy	1150.29	1003.22	941.52	690.11	677.42	

TABLE V. Comparison between experiment and theory for allowed and forbidden transitions. All values are in eV.

Line	Levels	Experiment	Error	Theory	Expt.−theory
$L\alpha_1$	$2p_{3/2}$-$3d_{5/2}$	4 110.09	0.02	4 109.92	0.17
$L\alpha_2$	$2p_{3/2}$-$3d_{3/2}$	4 097.38	0.03	4 097.23	0.15
$L\beta_1$	$2p_{1/2}$-$3d_{3/2}$	4 417.67	0.03	4 417.46	0.21
$L\beta_3$	$2s_{1/2}$-$3p_{3/2}$	4 512.03	0.03	4 511.78	0.25
$L\beta_4$	$2s_{1/2}$-$3p_{1/2}$	4 450.33	0.03	4 450.08	0.25
$L\eta$	$2p_{1/2}$-$3s_{1/2}$	3 958.37	0.05	3 957.28	1.09
Ll	$2p_{3/2}$-$3s_{1/2}$	3 638.01	0.04	3 637.05	0.96
$K\alpha_1$	$1s_{1/2}$-$2p_{3/2}$	29 778.69	0.10	29 778.61	0.08
$K\alpha_2$	$1s_{1/2}$-$2p_{1/2}$	29 458.16	0.05	29 458.38	−0.22
$K\beta_1$	$1s_{1/2}$-$3p_{3/2}$	33 624.13	0.12	33 624.42	−0.29
$K\beta_3$	$1s_{1/2}$-$3p_{1/2}$	33 563.10	0.12	33 562.73	0.37
	$1s_{1/2}$-$2s_{1/2}$	29 112.44	0.24	29 112.65	−0.21
	$1s_{1/2}$-$3s_{1/2}$	33 416.62	0.06	33 415.66	0.96
	$1s_{1/2}$-$3d_{3/2}$	33 875.95	0.08	33 875.84	0.11
	$1s_{1/2}$-$3d_{5/2}$	33 888.78	0.10	33 888.53	0.25

C. Theoretical uncertainties

The theoretical uncertainty is a combination of the uncertainty of one-electron calculations with an extended nucleus (mainly due to an uncertainty in the nuclear radius) and of a fraction of the self-energy screening correction. A fraction of 20% of this screening is compatible with theoretical results [48] on three-electron ions. The uncertainties on K-X intervals are of the order of 1 eV, and are dominated by the self-energy screening contribution. The L-line energy uncertainty is mainly dominated by uncalculated higher-order Auger shifts. The most uncertain level is the M_{l-1} due to a larger Auger shift. Contributions to theoretical ionization energies are displayed in Table IV. Theoretical transition energies and their differences with individual experimental values for all the K lines, L lines, and K-L and K-M differences are displayed in Table V.

D. Comparison with other calculations

The most detailed calculations of some of the inner-shell vacancies for Xe considered here have been performed by Chen et al. [27]. Level energy shifts due to Coster-Kronig fluctuations were given for $2s$, $3s$, and $3p$ holes. This is a subclass of the core-core and Auger shifts in the present work. In addition such core-core contributions where one, or both, of the holes in the intermediate state lie below the initial hole have been considered in this calculation. Such effects give the entire contribution, -2.7 eV, to a $2p_{3/2}$ hole and contribute with -2.0, -2.6, and -2.9 eV to holes in $2p_{1/2}$, $3p_{1/2}$, and $3p_{3/2}$, respectively. The results presented here demonstrate also the importance of treating the core-core effects relativistically. Especially when both of the intermediate-core holes lie above the initial hole, the result is sensitive to small changes in orbital energy due to the fact that important contributions arise when the energy denominator is very small. Thus the results for the different fine-structure levels can be rather different. For a $3p_{1/2}$ hole, for example, these latter effects contribute -3.0 eV while

the shift is only -2.0 eV for a $3p_{3/2}$ hole. Relativistic correlation and Breit correlation were not considered in Ref. [27].

IV. RESULTS AND CONCLUSION

Measurement results and corresponding transition-energy calculations are displayed in Table V. In conversions between wavelength and energy, the value $\lambda = 1239.842\,44$ eV nm from the 1986 adjustment of fundamental constants [24] was used. Most differences between experiment and theory are of the order of or below a few 0.1 eV. We believe this is the first time such a level of accuracy has been reached in the prediction of inner-shell transitions. These results clearly show that, if one can avoid difficulties due to solid-state effects for atoms with a single open shell, difficulties due to the relativistic many-body effects and QED corrections can be overcome.

The only lines for which a difference of the order of 1 eV is observed are those involving a $3s$ hole as initial or final state ($L\eta$, Ll, and $1s$-$3s$, with respective shift of 1.09, 0.96, and 0.96 eV). This is not unexpected from a theoretical point of view, as discussed earlier. The $3s$ is the level that is the most sensitive to Auger shift.

In this paper we have reported high-precision measurements of the positions of the prominent L-series lines in xenon and their profiles. Except for $L\alpha_1$, these lines do not appear in the usual compilations, and even this line was (properly) listed with a large uncertainty. Considerable care was exercised in the measurements in order to minimize and estimate in detail the errors. The present results are in generally good agreement with the only other recent group of measurements [12] which are as yet unpublished. The lines were produced by a very clean excitation procedure and in a gas-phase source. We have shown that under those circumstances even transitions involving strongly autoionizing states are suitable for detailed comparison with theory. We also presented data for the prominent K-series lines derived from earlier measurements [5] by correction for changes in the assumed

values of fundamental constants and a previously erroneous value for the lattice period of silicon. On the theoretical side we have reported the first highly detailed relativistic calculation of inner-shell hole states. Electrostatic and magnetic correlations, as well as core-core contributions (which were shown to be as important as the correlation contributions) have been calculated in the framework of relativistic many-body perturbation theory. We evaluated Auger shifts to second order. The present results seem more reliable than those of earlier works by Chen, Crasemann, and co-workers [27,28]. Preliminary results on higher-order corrections seem to indicate that further improvement can be made at the level of the many-body corrections. Improved self-energy screening is on the way and should also reduce residual discrepancies [48].

ACKNOWLEDGMENTS

APPENDIX A:
CRYSTAL SPACING DETERMINATIONS

Comparison of experimental x-ray data with theoretical estimates requires that the scale used for x-ray measurements be robustly connected to the Rydberg constant since the greater part of the term energies involved is expressed in this unit. This connection is nowadays realized in a three-step process. First, the lattice period of a silicon monocrystal is measured by combined x-ray and optical interferometry of a common baseline using an iodine-stabilized He-Ne laser as a reference; since this laser is the reference for all recent Rydberg determinations, the needed anchor is secured. Second, crystals suited to the intended spectroscopy are calibrated in terms of the initial Si artifact (or, more practically, specimens extracted from neighboring parts of the same boule) by a procedure which is not limited by x-ray line shape. Third, the crystals obtained in this way are used in self-calibrating angle-measuring engines to determine x-ray wavelengths via the Bragg-Laue relation as described in the text. This first appendix attends to matters concerning the initial x-ray/optical interferometric measurement, the XROI experiment, and the transfer of this initial calibration to other crystals required for the reported spectroscopy. A second Appendix, B, attends to some details of the calibration procedures required in the two instruments used in the work reported here

1. Optical interferometry of a Si lattice period

The main features of this measurement are the use of x-ray moiré fringes which directly reflect the crystal periodicity, independently of x-ray wavelength, and the

use of Fabry-Pérot optics to obtain high pointing precision in the optical channel. These two forms of interferometry are used to simultaneously mark repeated traversals of a common baseline. In recent years other interferometers have been added to evaluate deviation of the actual trajectory of motion from its ideal rectilinear form.

a. Resolution of previous problems

Results from this laboratory for the Si(220) lattice period [50,51] reported in the mid-1970s with a claimed accuracy of about 0.3 ppm were significantly discordant (1.8 ppm) with those subsequently obtained by workers at the Physikalisch-Technische Bundesanstalt (PTB) [52]. A renewed experiment here with added diagnostics showed that the earlier results obtained here were, in fact, incorrect due to a mistaken interpretation of the trajectory characterization used earlier and that the magnitude of the discrepancy could be approximately understood [14]. Since that time, persistent efforts have been maintained to produce a new measurement of significantly higher accuracy as described in the following subsection.

b. Current status of the XROI measurement

The improved apparatus, XROI-II, has been in operation since about 1988 with continuing effort to obtain reproducibility and understand systematic effects to a level consistent with available precision and the limitations of crystal quality. Although these efforts have not reached a fully satisfactory conclusion as yet, they are nonetheless sufficient for the purposes at hand.

In the early phase, data were characterized by reasonably good short-term reproducibility (better than 0.1 ppm) but much poorer long-term stability. This state of affairs was summarized in 1988 [53] and a tentative new value offered for the lattice period of the sample in hand. The lack of statistical control seemed to invite more rigorous study which revealed an unexplained systematic residue pattern whose magnitude suggested a possible association between the long-term instability noted earlier and the systematic residue pattern, itself not understood [54].

Since the last summary, the Fabry-Pérot optics were replaced giving much greater efficiency and pointing precision in the optical measurement. It appears that the troublesome systematic residue pattern has diminished and that the long-term inconsistency has similarly been reduced. Unfortunately, several other problems developed in the recent past so that a fully satisfactory measurement is still not at hand. However, on the basis of several small groups of measurements obtained over the past few months, a mean d spacing of 0.192 015 56(3) nm is currently estimated. This value is numerically consistent with the earlier preliminary value of 0.192 015 54 nm [53]. It is also consistent with the results of a direct comparison between the silicon used in XROI and a sample from the PTB [54] and, of course, the original 1.8 ppm discrepancy.

2. Transfer of calibration to other crystals

While we have by now established a dedicated instrument for comparison of crystals having nearly equal lattice spacings, the actual values of the Ge(220) and Si(220) spacings reflect the results of an earlier generation device. In both cases, however, the added contribution to uncertainty in reported values of transition energies owing to the lattice transfer is negligible.

a. Silicon (220) crystals for K-series spectra

Comparison of the interferometrically measured Si crystal (standard) with the Si crystals used for the K-series measurements (unknown) was performed using a two-crystal "nondispersive" Laue geometry. The standard and the unknown crystals are alternately placed in the second crystal position and are compared to the first long crystal which serves as a temporary reference. By subtraction, all properties of the first long crystal are eliminated and only the ratio of the lattice spacing of the unknown to the standard remains. The angular interval using x-ray paths at the two ends of the first long crystal is a measure of the lattice-spacing difference between the first and second crystals. Detailed crystal geometry is shown in Ref. [13].

In the measurement of the Si crystals used in the K-series measurements, Ag K radiation was used with a Si(440) crystal in the first position. The (440) planes were also used in the second crystals. The measured ratio (unknown/standard) at 22.5 °C is 0.999 999 83 (0.1 ppm).

b. Germanium (220) crystals for L-series spectra

Comparison of the interferometrically measured Si crystal to the Ge crystals used for the L-series spectra is more of a problem because of the large difference in lattice spacing. At the cost of an additional measurement step, comparison of Si to Ge was carried out using intermediate Si and Ge crystals cut so that planes having nearly equal spacing are available In the first step, Mo K radiation was used with a Si(355) crystal in the first position. The second crystals were alternately a Si(355) crystal and a Ge(800) crystal. In the second step, Ag K radiation was used with a Si(440) crystal in the first position. Here, the second crystal was alternately a Si(440) taken from the same boule as the Si(355) crystal and the interferometrically measured Si(440) crystal. By combining the ratios obtained in the two steps, the ratio (unknown-Ge/standard-Si) of 1.041 758 87 (0.1 ppm) at 22.5 °C was obtained.

The Ge crystals used in the L-series measurements and the Ge sample used in this comparison were taken from different boules. Pending a comparison involving a sample from the unmeasured Ge boule, we make the assumption that the lattice spacing of crystals from the two Ge boules are nearly equal. This assumption is likely to be correct below 1 ppm which would have a negligible effect on the results presented here.

APPENDIX B:
ANGLE SCALE CALIBRATIONS

Although the measurement and calibration schemes for the instruments used for K-series and L-series spectra differ considerably in refinement and operation, the underlying concepts are the same. In addition, we benefit from a certain synergism in that a byproduct of the transmission instrument's calibration serves as a "standard" for verifying angular calibration of the vacuum instrument.

1. The transmission two-crystal instrument

As described in the main text, this instrument is equipped with sine-measuring interferometers using a refined interpolation scheme capable of sensing angular changes near the level of 0.1 milliarcsec. These interferometers have an active range of about 30° but evidently we require a robust procedure for establishing the relationship between angles observed in optical fringe units and the fundamental angle, namely 2π radians.

The procedure we have developed uses an optical polygon whose mean interfacial angle is smaller than the range of the angle interferometers but is otherwise unrestricted. In particular, no assumption is made about the accuracy of the polygon except that the optical quality of its facets permits a good signal from a null-pointing autocollimator [55].

The stationary autocollimator identifies a direction to which pairs of adjacent polygon facets are successively aligned. Between such alignments, the angle interferometer evaluates the rotation in optical fringe units (and fractions thereof). This procedure is repeated for all pairs of successive polygon facets. With the needed arc-sine transformation, these observations amount to measurements of all the external angles of the polygon in arbitrary units (optical fringes). If the polygon facets are not excessively tipped relative to the axis about which it is rotated, then the sum of all external angles must equal a complete rotation, 2π radians or 360°. This constraint is sufficient to evaluate the calibration parameter which relates fringe units to angle units. Incidently, the measurements of individual interfacial angles carried out in this process calibrate the polygon's errors, permitting it to be used as a standard for assessing the accuracy of a lesser measuring engine as described next.

2. The vacuum two-crystal instrument

The angle encoder belonging to the second crystal's axis was calibrated using an optical polygon calibrated in the procedure described above and an offset-measuring autocollimator. This autocollimator function was realized by combining a null-pointing autocollimator [55] with a rotating wedge. The errors within a single encoder cycle (108 arcsec) showed an overall harmonic distribution with a peak-to-peak amplitude of approximately 7 arcsec which apparently arose because the sin/cos model for the signal output versus angle is an inadequate approximation. Several thousand encoder periods (each covering a range of 108 arcsec) were completely profiled

while comparing the encoder's interpolated output and the autocollimator readings. These patterns did not depend strongly on encoder phase and were fit to a sum of sine functions, the resulting function being used to linearize the interpolation algorithm. With this source of error under control, polygon calibrations showed no significant low-order harmonics in their overall pattern.

To ascertain the reading precision, a pair of mirrors were affixed to a caliperlike mount which could be set to (fixed) arbitrary angles between the mirror normals. When the encoder (with properly linearized interpola-

tion) was used with a null-pointing autocollimator, we were able to sample measurement reproducibility for a number of angular intervals around the encoder. The distribution of results was found to be roughly Gaussian with a standard deviation of 0.86 arcsec. Since the quantity measured is twice the Bragg angle, the effective error is only half this figure. In addition there is some component due to cultural noise effects on the position of the axis and the pointing instability of the autocollimator. Altogether it appears reasonable to assign an estimate of approximately 0.3 arcsec to the circle-reading instability.

*Present address: Advanced Photon Source, Bldg. 362, Argonne National Laboratory, 9700 S. Cass Avenue, Argonne, Il 60439.

†Present address: LPAN (URA 771 du CNRS), Boîte 93, Université Pierre et Marie Curie, 4 Place Jussieu, F-75252 Paris CEDEX 05, France.

[1] R. D. Deslattes, E. G. Kessler, Y.-K. Kim, and P. Indelicato, J. Phys. (Paris) Colloq. **48**, C9-591 (1987).

[2] P. Indelicato, *X-Ray and Inner-Shell Processes*, Proceedings of the Conference on X-Ray and Inner-Shell Processes, Knoxville, 1990, AIP Conf. Proc. No. 215, edited by T. Carlson, M. Krause, and S. Manson (AIP, New York, 1990), p. 591.

[3] T. Mooney (private communication).

[4] J. A. Bearden, Rev. Mod. Phys. **39**, 78 (1967).

[5] E. G. Kessler, Jr., R. D. Deslattes, D. Girard, W. Schwitz, L. Jacobs, and O. Renner, Phys. Rev. A **26**, 2696 (1982).

[6] R. D. Deslattes and E. G. Kessler, in *Atomic Inner-Shell Physics*, edited by B. Crasemann (Plenum, New York, 1985), p. 181.

[7] B. J. McKenzie, I. P. Grant, and P. H. Norrington, Comput. Phys. Commun. **21**, 233 (1980).

[8] I. P. Grant, B. J. McKenzie, P. H. Norrington, D. F. Mayers, and N. C. Pyper, Comput. Phys. Commun. **21**, 207 (1980).

[9] J. P. Desclaux, Phys. Scr. **21**, 436 (1980).

[10] J. P. Desclaux, Comput. Phys. Commun. **9**, 31 (1975).

[11] P. Indelicato and J. P. Desclaux, Phys. Rev. A **42**, 5139 (1990).

[12] R. LaVilla (private communication). The angle encoder calibration procedure employed in these measurements did not take into account errors within a single encoder cycle.

[13] R. D. Deslattes, E. G. Kessler, W. C. Sauder, and A. Henins, Ann. Phys. (N.Y.) **129**, 378 (1980).

[14] R. D. Deslattes, M. Tanaka, G. L. Greene, A. Henins, and E. G. Kessler, Jr., IEEE Trans. Instrum. Meas. **IM-36**, 166 (1987).

[15] R. D. Deslattes, B. G. Simson, and R. E. Lavilla, Rev. Sci. Instrum. **37**, 596 (1966).

[16] R. D. Deslattes and B. G. Simson Rev. Sci. Instrum. **37**, 753 (1966).

[17] R. D. Deslattes, Rev. Sci. Instrum. **38**, 616 (1967).

[18] R. D. Deslattes, Nucl. Instrum. Methods Phys. Res. B **31**, 51 (1988).

[19] F. James and M. Roos, Comput. Phys. Commun. **10**, 343 (1975).

[20] J. A. Bearden, A. Henins, J. G. Marzolf, W. C. Sauder, and J. S. Thomsen, Phys. Rev. A **135**, 899 (1964).

[21] A. E. Sandström, in *Experimental Methodology of X-Ray*

Spectroscopy, edited by S. Flügge, Encyclopedia of Physics Vol. 30 (Springer-Verlag, Berlin, 1957), p. 78.

[22] D. T. Cromer and D. Liberman, J. Chem. Phys. **53**, 1891 (1970).

[23] E. G. Kessler and R. D. Deslattes, IEEE Trans. Nucl. Sci. **NS-30**, 991 (1983).

[24] E. R. Cohen and B. N. Taylor, Rev. Mod. Phys. **59**, 1121 (1987).

[25] B. Crasemann, K. R. Karim, and M. H. Chen, At. Data Nucl. Data Tables **36**, 356 (1987).

[26] M. H. Chen, B. Crasemann, M. Aoyagi, K.-N. Huang, and H. Mark, At. Data Nucl. Data Tables **26**, 561 (1981).

[27] M. H. Chen, B. Crasemann, N. Martensson, and B. Johansson, Phys. Rev. A **31**, 556 (1985).

[28] M. H. Chen, B. Crasemann, and H. Mark, Phys. Rev. A **24**, 1158 (1981).

[29] P. Indelicato, O. Gorceix, and J. P. Desclaux, J. Phys. B **20**, 651 (1987).

[30] W. R. Johnson and G. Soff, At. Data Nucl. Data Tables **33**, 405 (1985).

[31] P. Indellicato, J. Phys. B **19**, 1719 (1986).

[32] S. Love, Ann. Phys. (N.Y.) **113**, 153 (1978).

[33] J. Sucher, J. Phys. B **21**, L585 (1988).

[34] I. Lindgren, J. Phys. B **23**, 1085 (1990).

[35] P. Indelicato, J. Phys. (Paris) Colloq. **50**, C1-239 (1989).

[36] S. Salomonson and P. Öster, Phys. Rev. A **40**, 5559 (1989).

[37] S. Salomonson and P. Öster, Phys. Rev. A **40**, 5548 (1989).

[38] R. L. Chase, H. P. Kelly, and H. S. Köhler, Phys. Rev. A **3**, 1550 (1971).

[39] H. P. Kelly, Phys. Rev. A **11**, 556 (1975).

[40] T. Beier and G. Soff, Z. Phys. D **8**, 129 (1988).

[41] P. J. Mohr, Ann. Phys. (N.Y.) **88**, 52 (1974).

[42] P. J. Mohr, Phys. Rev. A **26**, 2338 (1982).

[43] P. J. Mohr and Y.-K. Kim (private communication).

[44] P. Indelicato, Nucl. Instrum. Methods Phys. Res. B **31**, 14 (1988).

[45] P. Indelicato, J. Phys. (Paris) Colloq. **48**, C9 (1987).

[46] A. M. Desiderio and W. R. Johnson, Phys. Rev. A **3**, 1267 (1971).

[47] G. W. Drake, Can. J. Phys. **66**, 586 (1988).

[48] P. Indelicato and P. J. Mohr (unpublished).

[49] P. L. Altick and E. N. Moore, Phys. Rev. **147**, 59 (1966).

[50] R. D. Deslattes, A. Henins, H. A. Bowman, R. M. Schoonover, C. L. Carrol, I. L. Barnes, L. A. Machlan, L. J. Moore, and W. R. Schields, Phys. Rev. Lett. **33**, 463 (1974).

[51] R. D. Deslattes, A. Henins, R. M. Schoonover, C. L. Carrol, and H. A. Bowman, Phys. Rev. Lett. **36**, 898 (1976).

[52] P. Becker, K. Dorenwendt, G. Ebeling, R. Lauer, W. Lucas, R. Probst, H.-J. Rademacher, G. Reim, P. Seyfried,

and H. Siegert, Phys. Rev. Lett. **46**, 1540 (1981).

[53] R. D. Deslattes, in *The Art of Measurement. Metrology in Fundamental and Applied Physics,* edited by B. Kramer (VCH, Weinheim, 1988), p. 193.

[54] R. D. Deslattes and E. G. Kessler, IEEE Trans. Instrum. Meas. **IM-40**, 92 (1991).

[55] G. G. Luther, R. D. Deslattes, and W. R. Towler, Rev. Sci. Instrum. **55**, 747 (1984).